

Alma Mater Studiorum Università di Bologna
Archivio istituzionale della ricerca

Conical Intersection Passages of Molecules Probed by X-ray Diffraction and Stimulated Raman Spectroscopy

This is the final peer-reviewed author's accepted manuscript (postprint) of the following publication:

Published Version:

Conical Intersection Passages of Molecules Probed by X-ray Diffraction and Stimulated Raman Spectroscopy / Nam Y.; Keefer D.; Nenov A.; Conti I.; Aleotti F.; Segatta F.; Lee J.Y.; Garavelli M.; Mukamel S.. - In: THE JOURNAL OF PHYSICAL CHEMISTRY LETTERS. - ISSN 1948-7185. - ELETTRONICO. - 12:51(2021), pp. 12300-12309. [10.1021/acs.jpcclett.1c03814]

Availability:

This version is available at: <https://hdl.handle.net/11585/844751> since: 2022-01-11

Published:

DOI: <http://doi.org/10.1021/acs.jpcclett.1c03814>

Terms of use:

Some rights reserved. The terms and conditions for the reuse of this version of the manuscript are specified in the publishing policy. For all terms of use and more information see the publisher's website.

This item was downloaded from IRIS Università di Bologna (<https://cris.unibo.it/>).
When citing, please refer to the published version.

(Article begins on next page)

Cite this: DOI: 00.0000/xxxxxxxxxx

Conical Intersection Passages of Molecules Probed by X-ray Diffraction and Stimulated Raman Spectroscopy

Yeonsig Nam,^{*a,b} Daniel Keefer,^a Artur Nenov,^c Irene Conti,^c Flavia Aleotti,^c Francesco Segatta,^c Jin Yong Lee,^{*b,d} Marco Garavelli,^c and Shaul Mukamel ^{*a}

Received Date

Accepted Date

DOI: 00.0000/xxxxxxxxxx

Conical intersections (CoIns) play an important role in many ultrafast relaxation channels in molecules. Their monitoring remains a formidable experimental challenge. We theoretically compare the probing of the CoIn passage in 4-thiouracil by monitoring its vibronic coherences, using off-resonant X-ray stimulated Raman spectroscopy (TRUECARS) and time-resolved X-ray diffraction (TXRD) enabled by free-electron laser pulses. The two techniques reveal complementary information about the non-adiabatic passage with adequate spectral and temporal resolutions. The signals are simulated for the photorelaxation from the optically bright S_2 to the dark S_1 state using quantum nuclear wavepacket (WP) dynamics. Upon photoexcitation, the WP oscillates between the Franck-Condon point, the S_2 minimum, and the CoIn with a 70 fs period. A vibronic coherence first emerges at 20 fs and is observable until the S_2 state is fully depopulated. The distribution of the vibronic frequencies involved in the coherence is recorded by the TRUECARS spectrogram. In turn, the TXRD signal provides spatial images of electron densities associated with the CoIn. In combination, the two signals provide a detailed picture of CoIn pathways which helps to study underlying photophysics in thiobases.

1 Introduction

Probing conical intersection (CoIn) dynamics is important to unravel the rates and outcomes of many photophysical and photochemical processes in molecules. At CoIns, two or more electronic surfaces become degenerate and the electronic and nuclear degrees of freedom become strongly coupled since the Born-Oppenheimer picture breaks down. This opens up ultrafast non-radiative decay channels for excited molecules. Several techniques, such as transient vibrational/visible absorption^{1–4} and

photoionization spectra⁵, have been applied to observe CoIns through indirect signatures, i.e. a change of absorption lines. Detecting unique signatures that directly emerge from CoIn dynamics remains an open challenge.

Free-electron X-ray light sources (FEL) offer a novel window into CoIn dynamics^{6,7} thanks to their unique temporal and spatial resolutions. Transient Redistribution of Ultrafast Electronic Coherences in Attosecond Raman signals (TRUECARS) has been proposed for the direct monitoring of the CoIn passage⁸. A hybrid X-ray probe field composed of a femtosecond narrowband and an attosecond broadband pulse provides a phase-sensitive detection of the electronic Raman transition at the CoIn via a core excited state. The same information can be obtained by covariance signals with stochastic X-ray pulses⁹. TRUECARS has been employed theoretically to unveil the CoIn dynamics of uracil^{9,10}, thiophenol^{11,12}, and a bichromophoric heterodimer¹³.

In a different technique, time-evolving electronic charge densities at CoIn passage can be imaged with subfemtosecond resolution using ultrafast time-resolved X-ray diffraction (TXRD)^{14–16}. Traditionally, X-ray diffraction has been primarily used to study stationary molecular samples by elastic scattering from the ground state electron densities^{17,18}. In contrast, photoexcited molecules are prepared in a time-evolving superposition of states, and inelastic scattering from different electronic states as well as electronic and vibrational coherences contribute to the signal¹⁹.

^a Department of Chemistry, University of California, Irvine, California 92697-2025, United States

^b Convergence Research Center for Energy and Environmental Sciences, Sungkyunkwan University, Suwon 16419, Korea

^c Dipartimento di Chimica Industriale “Toso Montanari,” Università degli Studi di Bologna, I-40136 Bologna, Italy

^d Department of Chemistry, Sungkyunkwan University, Suwon 16419, Korea

*yeonsign@uci.edu, jinyilee@skku.edu, smukamel@uci.edu

† Electronic Supplementary Information (ESI) available: (1) Derivation of the TRUECARS and TXRD signal; (2) Loop diagram rule; (3) Supplementary results and discussions; (4) Supplementary figures: Optimized geometry for the FC, S_1 min, S_2 min, projection of gradient on S_1 and S_2 PES, CoIn, NAC and transition polarizabilities, nuclear wavepacket movie, TRUECARS signal along $x/y/z$, axis, TRUECARS signal upon different Gobbler, real space electron densities, loop diagrams for x-ray scattering, three dimensional diffraction signal movie, Two dimensional diffraction signal along q_{xy}/q_z planes, time-resolved diffraction signal along $q_x/y/z$ /rad, and ratio of the coherence contribution compared to the total TXRD signal. See DOI: 00.0000/00000000.

Hence, TXRD can provide additional information on the CoIn passage: the momentum space image allows the reconstruction of the real-space charge density profile once the phase problem is solved²⁰.

Thiouracils are nucleobases where one or more carbonyl oxygen atoms of uracil are substituted by sulfur atoms. Thionation redshifts the visible absorption spectra and alters their photo-physics compared to their unsubstituted counterpart²¹: they undergo intersystem crossing (ISC) to long-lived triplet states^{22,23} contrary to uracil which undergoes ultrafast nonradiative relaxation to the ground state^{9,10,24,25}. Thanks to their high triplet quantum yield^{23,26}, thiouracils have attracted significant biological relevance such as site-specific photoprobe for photodynamic therapy^{27,28}, and photoinduced cross-linkers^{29,30}. Moreover, they provide a good model system for unravelling how a single-atom substitution (and the location of the substitution) affects the energy relaxation pathway of DNA/RNA nucleobases. However, the nonadiabatic passage from the bright $\pi\pi^*$ state to the dark $n\pi^*$ state of 4-thiouracil is largely unexplored which is prototypical for all other canonical and many modified nucleo(thio)bases. It is the primary event after UV absorption and the ongoing nuclear dynamics through the initial CoIn determines fundamental properties like the photostability of the nucleo(thio)bases²⁴. Hence, it is a key issue to be addressed prior to unravelling the role of $n\pi^*$ state as a doorway to the long-lived triplet manifold.

In this article, we study complementary information about the CoIn passage revealed by the TRUECARS and TXRD techniques. The former directly probes the timing and the energetic distributions of vibronic coherences while the latter gives spatial images of the electron densities passing through the CoIns.

2 Simulation Details

2.1 Quantum Chemistry

The potential energy surfaces (PESs) for the adiabatic states were calculated using OpenMOLCAS program³¹ at the state-average CASSCF level of theory followed by the second order perturbation (CASPT2)³² employing an active space of 12 electrons in 9 orbitals (5 π , one sulfur lone pair n , and 3 π^* orbitals) by taking three lowest adiabatic electronic states into account (SS-CASPT2/SA-3-CASSCF(12,9)). The CASPT2 calculations were performed with the single state (SS) flavor, using an imaginary shift of 0.2 and setting the IPEA shift to 0.0. The ANO-L basis set³³ was used, with contractions 5s4p2d1f on sulfur, 4s3p2d1f on carbon, oxygen, nitrogen atoms, and 3s2p1d on hydrogen atoms.

The geometry of the Franck-Condon point (FC) is optimized at the MP2 level, whereas the geometries of the S_1 minimum (S_1 min), S_2 minimum (S_2 min), and the S_2/S_1 conical intersection (CoIn) are optimized at SS-CASPT2/SA-3-CASSCF(12,9) level with the COMBRAMM interface³⁴ with OpenMolcas as shown in Fig. S1. The optimized geometries and the electronic energies at the FC, the CoIn and the S_2 min calculated with CASSCF, SS-CASPT2, and XMS-CASPT2 are compared and discussed in the ESI. The FC, the S_2 min, and the S_2/S_1 CoIn structures were then used to construct two nuclear degrees of freedom for our effective

Hamiltonian^{24,35}. The first coordinate $\mathbf{v}_{\text{FC} \rightarrow \text{CoIn}}$ is the normalized displacement vector that points from the FC to the CoIn. $\mathbf{v}_{\text{FC} \rightarrow S_2 \text{ min}}$ is the displacement vector from the FC to the local S_2 min which is then orthonormalized with respect to $\mathbf{v}_{\text{FC} \rightarrow \text{CoIn}}$. Nonadiabatic couplings (NACs) were computed analytically at the SA-3-CASSCF(12,9) level, and then were corrected (i.e. uniformly rescaled) by a scaling factor equal to the ratio between the CASSCF and the CASPT2 energy difference between S_2 and S_1 states.

The state and transition densities $\sigma(\mathbf{q}, \mathbf{R})$ were evaluated in 0.1 increments for both $\mathbf{v}_{\text{FC} \rightarrow \text{CoIn}}$ and $\mathbf{v}_{\text{FC} \rightarrow S_2 \text{ min}}$ coordinates, giving $16 \times 11 = 176$ total of the grid points. They were evaluated from the state specific charge density matrices P_{rs}^{ij} (calculated using the CASSCF wavefunctions) according to

$$\sigma_{ij}(\mathbf{q}, \mathbf{R}) = \int d\mathbf{r} e^{-i\mathbf{q}\mathbf{r}} \sum_{rs} P_{rs}^{ij}(\mathbf{R}) \phi_r^*(\mathbf{r}, \mathbf{R}) \phi_r(\mathbf{r}, \mathbf{R}), \quad (1)$$

using the basis set of atomic orbitals $\phi_r(\mathbf{r})$. There are a total of 300 $\phi_r(\mathbf{r})$ for 4-thiouracil (4TU) (30 for each nitrogen, carbon, and oxygen, 34 for sulfur, and 14 for each hydrogen). All 66 electrons of 4TU contribute to the diagonal state densities, σ_{ii} , while the transition density σ_{ij} consist of one electron located in the sulfur lone pairs.

2.2 Wavepacket Simulations

The PESs and all molecular quantities are discretized on a spatial grid of 128x128 grid points in $\mathbf{v}_{\text{FC} \rightarrow \text{CoIn}}$ and $\mathbf{v}_{\text{FC} \rightarrow S_2 \text{ min}}$ by inter/extra-polation. Nuclear wavepacket simulations are then performed by numerically integrating the time-dependent Schrodinger equation³⁶:

$$i\hbar \frac{\partial}{\partial t} \psi = \mathbf{H} \psi = \left[\mathbf{T}_v + \mathbf{V} \right] \psi, \quad (2)$$

with the kinetic energy operator \mathbf{T}_v of the nuclei in internal coordinates \mathbf{v} , the potential energy operator \mathbf{V} . The time-dependent Schrodinger equation is solved exactly: the quantum nature of the nuclear wavepacket, e.g., geometric phase, and the bifurcation process at CoIn are fully captured³⁵. This is in contrast to more approximate approaches e.g., the multi-configurational time-dependent Hartree (MCTDH)³⁷ where the wavepacket is expressed by a sum of products of individual “configurations”, or ab-initio multiple spawning (AIMS)³⁸ that propagates Gaussian functions and spawns new ones at excited state crossings. We expand the total time-dependent molecular wavefunction $\psi(\mathbf{r}, \mathbf{R}, t)$ in the adiabatic basis

$$\psi(\mathbf{r}, \mathbf{R}, t) = \sum_i c_i(t) \chi(\mathbf{R}, t) \phi(\mathbf{r}, \mathbf{R}) \quad (3)$$

where $\chi(\mathbf{R}, t)$ is the normalized nuclear wavepacket in the adiabatic electronic state $\phi(\mathbf{r}, \mathbf{R})$, and c_i is the coefficient (amplitude) of adiabatic states. The starting wavepacket is obtained by impulsive excitation of the ground state vibrational wavefunction from S_0 to S_2 . The Chebychev propagation scheme³⁶ with a time step of 0.048 fs is employed to propagate this wavepacket until the final time of 242 fs. To set up the kinetic energy operator, the

G-matrix formalism³⁹ was employed as

$$\mathbf{T}_v \simeq -\frac{\hbar^2}{2m} \sum_{r=1}^M \sum_{s=1}^M \frac{\partial}{\partial \mathbf{v}_r} \left[\mathbf{G}_{rs} \frac{\partial}{\partial \mathbf{v}_s} \right] \quad (4)$$

with the G-matrix computed via its inverse elements

$$(G^{-1})_{rs} = \sum_{i=1}^{3N} m_i \frac{\partial \mathbf{x}_i}{\partial \mathbf{v}_r} \frac{\partial \mathbf{x}_i}{\partial \mathbf{v}_s} \quad (5)$$

In the case of the 4TU coordinates, the G-matrix elements are $G_{v_r v_r} = 0.00007234 a.u.$, $G_{v_s v_s} = 0.00009237 a.u.$, and the kinetic coupling $G_{v_r v_s} = -0.00002765 a.u.$. Our effective Hamiltonian is designed for describing the transition from the S_2 to the S_1 state and it may not be accurate to describe the WP propagation in the S_1 PES since other nuclear degrees of freedom not captured by our Hamiltonian become relevant. For example, $S_2 \rightarrow T_2 \rightarrow T_1$ or $S_2 \rightarrow S_1 \rightarrow T_1$ competitive pathways exist in 4-thiouracil (4TU)²². Population of the triplet manifold out of the S_2 or S_1 state cannot be described by our two-dimensional Hamiltonian since spin-orbit crossings are not readily accessible by the numerical protocol and the intersystem crossing may be facilitated along other modes. The former pathway can be controlled since it gives rise only to weak photoinduced absorption contribution²². Most part of the S_1 WP will be directed to the intersystem crossing (the latter pathway), and only a small part of S_1 WP will oscillate in our reactive coordinate. We thus employ a Butterworth⁴⁰ filter operation in the region of the S_1 min to absorb the parts of the WP which will otherwise decay to the triplet $\pi\pi^*$ state, preventing major artificial back-evolution to S_2 . The filter was of right-pass type and placed at $\mathbf{v}_{FC \rightarrow CoIn} = -0.1 a.u.$ with an order of 100.

3 Results and Discussion

We investigate the dynamics of 4TU upon impulsive photoexcitation to the $S_2(^1\pi\pi^*)$ state (the pump pulse is not explicitly included in the simulation). The potential energy surfaces of 4TU in a reduced two-dimensional (2D) nuclear space are displayed in Fig. 1. This space is spanned by two coordinate vectors $\mathbf{v}_{FC \rightarrow CoIn}$ and $\mathbf{v}_{FC \rightarrow S_2 min}$ which represent the linear displacement vectors from the FC to the S_2/S_1 CoIn, and from the FC to the S_2 min, respectively (See Fig. S1 in the SI). The gradients at the FC, the S_2 min, the S_1 min, and several points in the periphery of the PES was computed and projected onto our 2D reactive coordinates (Fig. S2). Our 2D subspace encloses a half of the full gradient except the upper left point (red point), where the total gradient mainly directs elongation of the two C-N bonds which is not described by our 2D spaces. As for the gradient of S_1 state, the total length and the direction of the projection shows the similar feature to the ones for S_2 . Notably, at its minimum, S_1 state has a projected length of 0.02 out of 0.05 total length, just as the S_2 in its respective minimum (0.02 out of 0.04). This implies that our nuclear space is comparably well set up to describe the wavepacket evolution in S_2 and its relaxation to S_1 (and to S_1 min) through the CoIn despite the S_1 min not considered in the generation of the coordinates. The ground state is not populated since our nuclear space does not cover the $S_1 \rightarrow S_0$ CoIn(s) passage, we thus refer CoIn to S_2/S_1 CoIn throughout the paper

unless otherwise specified.

In 4TU, the FC, the CoIn, the S_2 min and the S_1 min structure are all planar and the main structural difference is the C–S bond length and the relevant $\angle CCS$ angle (Fig. S1): FC (1.643 Å, 125.14°), S_2 min (1.861 Å, 129.79°), S_1 min (1.751 Å, 125.16°), and CoIn (1.996 Å, 134.58°). This supports that the $\mathbf{v}_{FC \rightarrow S_2 min}$, which is mainly the elongation of the C–S bond, could describe the CoIn to the S_1 min pathway to some extent. In 4TU, the S_2 PES exhibits a single well with a barrierless pathway from the FC through the S_2 min to the CoIn, but with the energy difference of 0.3 eV between the S_2 min and the CoIn. In contrast, unmodified uracil exhibits a double well in the excited state with a small 0.5 eV barrier between the S_2 min and the CoIn peaks and only a small part of the WP reaches the CoIn²⁴. This demonstrates how even a single atom substitution of 4TU compared to uracil can significantly influence the electronic structures and the relaxation dynamics. The nonadiabatic couplings (NACs) exhibit a characteristic sign change at the CoIn, due to switching of the electronic character of the adiabatic states (Fig. S3a).

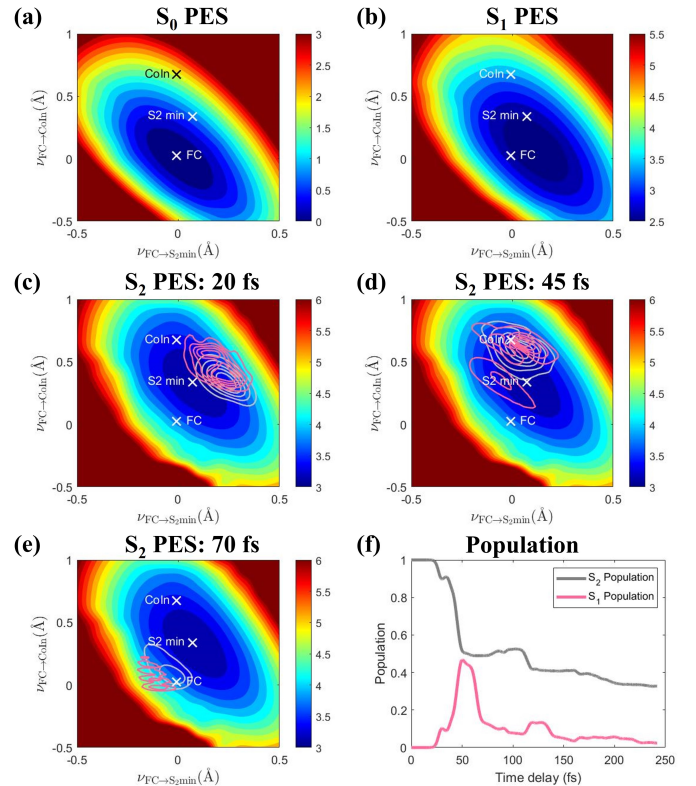


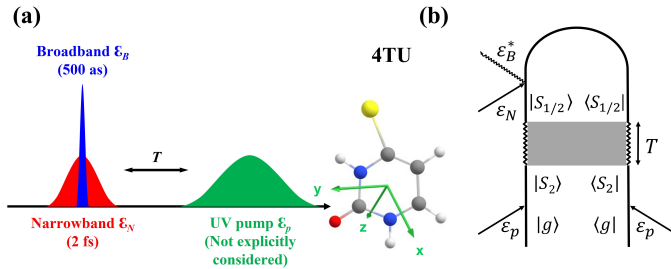
Fig. 1 Potential energy surfaces and nuclear wavepacket dynamics: (a) S_0 PES, (b) S_1 PES, S_2 PES with the nuclear wavepacket at (c) 20 fs, (d) 45 fs, and (e) 70 fs, and (f) the state populations. S_2 wavepacket (grey contours), S_1 wavepacket (pink contour). The complete movie including S_1 PES can be found in Fig. S4

Using the PESs and NACs, a nuclear WP was propagated by exactly solving the time-dependent Schrodinger equation for our effective Hamiltonian (the complete nuclear WP movies including S_1 PES can be found in Fig. S4). Upon photoexcitation, the WP starts at the FC region, and first reaches the S_2 min at 20 fs. The NAC is non-vanishing there, the S_1 electronic state is populated

and a vibronic coherence between S_2 and S_1 is created. The WP reaches the CoIn at 45 fs, where the NAC is strongest and the major CoIn relaxation takes place. The wavepacket bifurcates into S_2 and S_1 WPs with a significant overlap between them, creating a vibronic coherence. At 70 fs, the WPs evolve back to the FC region. Here, the presence of the $\mathbf{v}_{\text{FC} \rightarrow S_2 \text{min}}$ coordinate, despite being similar to the $\mathbf{v}_{\text{FC} \rightarrow \text{CoIn}}$ coordinate, facilitates decoherence after the CoIn passage: the two WPs evolve differently, and their overlap strongly decreases over time (see video Fig. S4 in the SI): the S_1 WP moves clockwise and reaches the CoIn at around 80 fs; the population is inversely transferred from the S_1 to the S_2 (Fig. 1f between 80 to 110 fs). The S_2 WP in contrast moves counterclockwise and both S_1 and S_2 WP overlap again at the CoIn at 115 fs. The WPs oscillate between the FC and the CoIn with a 70 fs period. The S_2 population decay is fitted with an exponential function, $P(t) = Ae^{-t/k} + P_0$, where A is a coefficient and P_0 is the initial population, yielding a time constant k of 56 fs. The relaxation time compares well with experiment (76 fs) and surface hopping simulations (67.5 fs)²² and is faster than that computed for uracil (186 fs)¹⁰ due to the absence of energy barriers.

3.1 TRUECARS

The vibronic coherence between S_2 and S_1 emerging at the CoIn is probed by the TRUECARS signal using the hybrid field \mathcal{E}_N (central frequency at 2450 eV with 2 fs duration) and \mathcal{E}_B (500 as duration), after the waiting time T (Sch. 1a). Other probe frequencies may be employed as long as it is off-resonant to any molecular transition. 350 eV has been used for uracil¹⁰, and ideas for potential signal enhancement by employing a pre-resonant probe frequency are given in Refs^{9 13}. The corresponding loop diagram is given in Sch. 1b.



Sch. 1 (a) Pulse configuration and (b) loop diagram for TRUECARS with randomly oriented 4-thiouracil. The pump pulse \mathcal{E}_p (not considered explicitly in the simulation) creates an electronic and nuclear population in the excited state S_2 . The grey area indicates a free evolution period of the molecule. At time delay T , the hybrid \mathcal{E}_B (broad) and \mathcal{E}_N (narrow) pulse is used to probe the dynamics. See SI and Ref⁴¹ for loop diagram rules.

The TRUECARS signal reads^{8,11},

$$S(\omega_s, T) = \text{Im} \int dt \mathcal{E}_B^*(\omega_s) \mathcal{E}_N(t-T) e^{i\omega_s(t-T)} \langle \alpha(t) \rangle \quad (6)$$

where "Im" denotes the imaginary part, $\mathcal{E}_{N/B}$ is a hybrid narrow/broadband Gaussian pulse envelope (Sch. 1a), ω_s is the carrier frequency, T is the time delay between the pump and the

probe. The S_2/S_1 transition polarizability $\alpha(t)$ is calculated from the transition charge density, $\sigma_{S_2S_1}$ (See the SI for derivation).

The TRUECARS signals were computed in the x, y, and z polarization direction in the molecular frame (Fig. S5) and then averaged to give the rotationally averaged TRUECARS signal shown in Fig. 2a. This signal selectively probes the vibronic coherence in a background-free manner: it does not show up until 20 fs when the vibronic coherence first emerges and the transition polarizabilities show up (Fig. 2b). At 45 fs, the TRUECARS signal reaches a maximum due to the maximal overlap of S_2/S_1 WPs and the large transition polarizabilities. After a decay period, the signal starts to re-appear at 80 fs when the parts of the S_1 WP that have not been absorbed have evolved back to the CoIn. The TRUECARS signal remains visible until after 200 fs due to the delocalized nature of the S_2 WP, where its tail continue to reach the CoIn.

To verify the use of the artificial placement of Gobbler at the S_1 min and its impact on the TRUECARS signal, we performed nuclear wavepacket dynamics simulations by changing the location of the Gobbler (Fig. S6). We find that placing the Gobbler closer the CoIn (Fig S6c-d) does not affect the signals substantially. Placing Gobbler further below (Fig. S6b) from the S_1 min results in larger coherences since major parts of the S_1 wavepacket are not absorbed and evolve back to the CoIn. This leads to inverse-population-transfer to the S_2 state and a strong signal around 200 fs. How much of the S_1 wavepacket evolves back to the CoIn after passage through the S_1 min ultimately depends on the accessibility and efficiency of the intersystem crossing to the triplet state, not included in our simulation. The signal around 200 fs might be stronger or weaker than predicted by our simulations.

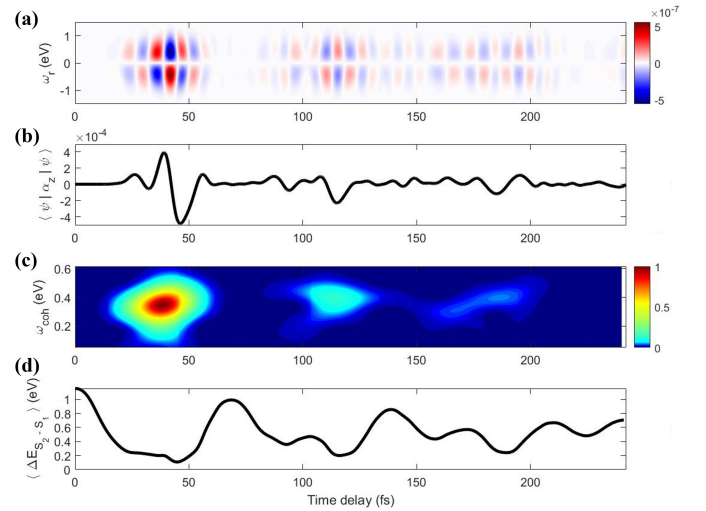


Fig. 2 TRUECARS signal of 4TU. (a) The frequency-dispersed signal $S(\omega_r, T)$, (b) Expectation value of the polarizability operator α_z , (c) Frequency-resolved optical-gating spectrogram (Eq. 7) with signal trace $S(t)$ taken at $\omega_r = 0.37$ eV (maximum signal intensity), (d) Expectation value of the energy splitting between S_2 and S_1 states, $\langle \Delta E_{S_2-S_1} \rangle = \langle \psi | E(S_2) - E(S_1) | \psi \rangle$.

The TRUECARS signal exhibits temporal Stokes and anti-Stokes

oscillations between positive and negative values at non-zero Raman shifts. The energetic nature of the adiabatic states in the vibronic coherence is encoded in the temporal oscillations of the frequency-dispersed signal. This is due to the dynamical phase imprinted in the coherence stemming from the energy difference between the adiabatic states^{8,10}. To visualize the dynamical evolution of this frequency, a temporal trace $S(t)$ at constant $\omega_r = 0.37$ eV, is convolved with a Gaussian gating function $E_{\text{gate}}(t)$ with 4.84 fs FWHM, obtaining a spectrogram resembling the frequency-resolved optical-gating (FROG) measurement⁴²:

$$I_{\text{FROG}}(T, \omega_{\text{coh}}) = \left| \int_{-\infty}^{\infty} dt S(t) E_{\text{gate}}(t - T) e^{-i\omega_{\text{coh}} t} \right|^2 \quad (7)$$

To analyze the energetic profiles, we had used Wigner¹⁰ and FROG⁹ and both give the spectrogram of the TRUECARs signal which contains the relevant information. The Spectrogram depicted in Fig. 2c exhibits strong features at 45, 115, and 185 fs. Between 100 and 200 fs, the main frequency feature first decreases to 0.4 eV and then slightly increases again, but maintains energy splitting of around 0.4 eV implying that the WP re-visits the same CoIn periodically. To further extend this analysis, we have computed the expectation value of the energy splitting between S_2 and S_1 , $\langle \Delta E_{S_2-S_1} \rangle = \langle \psi | E(S_2) - E(S_1) | \psi \rangle$, where $E(S_2)$ and $E(S_1)$ correspond to the potential energy surfaces of S_2 and S_1 state, respectively (Fig. 2d). The temporal profile of this expectation value coincides with the one of the FROG spectrogram, and with the motion of the WPs. The TRUECARs spectrogram thus provides information about the timing and the energetic profiles at the CoIn.

3.2 Time-resolved X-ray diffraction

TXRD images electron densities evolving in the vicinity of the CoIns. This spatial information is not accessible with TRUECARs, since it requires a scattering measurement. To image the CoIn dynamics by TXRD, we have computed the transition charge densities, $\sigma_{S_2S_1}(\mathbf{q}, \mathbf{R})$ on a grid across the two-dimensional nuclear space. The state densities $\sigma_{S_1S_1}$ and $\sigma_{S_2S_2}$ are spanned across the entire 4TU molecule and are virtually identical (Fig. S7). This is due to the fact that all 66 electrons contribute to the state densities whereas only a single active electron contributes to the electronic transition. The transition charge density $\sigma_{S_2S_1}$ is mainly located around the S atom.

The TXRD signals were computed in the three-dimensional momentum space, and then radially averaged to get the TXRD signal for a randomly oriented sample. The gas phase (single molecule) TXRD signal of a sample with N noninteracting molecules reads^{19,43,44}

$$S_1(\mathbf{q}, T) \propto N \int dt |\mathcal{E}_X(t - T)|^2 \tilde{S}_1(\mathbf{q}, t) \quad (8)$$

where

$$\begin{aligned} \tilde{S}_1(\mathbf{q}, t) &= \rho_{S_1S_1}(t) \langle \chi_{S_1}(t) | \sigma_{S_1S_1}^\dagger \sigma_{S_1S_1} | \chi_{S_1}(t) \rangle & (i) \\ &+ \rho_{S_2S_2}(t) \langle \chi_{S_2}(t) | \sigma_{S_2S_2}^\dagger \sigma_{S_2S_2} | \chi_{S_2}(t) \rangle & (ii) \\ &+ \rho_{S_1S_1}(t) \langle \chi_{S_1}(t) | \sigma_{S_1S_2}^\dagger \sigma_{S_2S_1} | \chi_{S_1}(t) \rangle & (iii) \\ &+ \rho_{S_2S_2}(t) \langle \chi_{S_2}(t) | \sigma_{S_2S_1}^\dagger \sigma_{S_1S_2} | \chi_{S_2}(t) \rangle & (iv) \\ &+ 2\text{Re}[\rho_{S_2S_1}(t) \langle \chi_{S_2}(t) | \sigma_{S_2S_2}^\dagger \sigma_{S_2S_1} | \chi_{S_1}(t) \rangle \\ &+ \rho_{S_2S_1}(t) \langle \chi_{S_2}(t) | \sigma_{S_2S_1}^\dagger \sigma_{S_1S_1} | \chi_{S_1}(t) \rangle] & (v) \end{aligned} \quad (9)$$

where each term corresponds to a specific loop diagram in Fig. S8. $\rho_{S_1S_1}$ and $\rho_{S_2S_2}$ are the electronic state populations, and $\rho_{S_2S_1}$ is the corresponding coherence. The first (i) and the second (ii) term in Eq. 9 represent elastic scattering from the first and the second excited state, respectively. The third (iii) and fourth (iv) term describe inelastic scattering from two states. The last term (v) represents the mixed elastic/inelastic scattering from vibronic coherences. The TXRD signal is presented after normalizing with the factor,

$$S_1(\mathbf{q}, T) = \frac{S_1(\mathbf{q}, T) - S_1(\mathbf{q}, T < 0)}{S_1(\mathbf{q}, T < 0)}. \quad (10)$$

The three-dimensional diffraction pattern and the projected diffraction signal integrating over \mathbf{q}_x , \mathbf{q}_y , or \mathbf{q}_z axis are presented in Fig. S9–10 and discussed in the ESI. The diffraction patterns show only a subtle changes over time, reflecting the absence of photochemical reaction upon optical excitation but merely a photophysical relaxation between electronic states; in photorelaxation of 4TU, no major conformational changes (e.g. cis-trans isomerization or bond breaking) in the molecule occur. Below, we focus on the contribution from vibronic coherence that gives information about the CoIn.

The total, radially-averaged diffraction signal is shown in Fig. 3a-b. The mixed (in)elastic scattering is a one-electron process, hence the radially averaged coherence term is weak and buried under the total diffraction signal where the all-electron elastic scattering contribution is dominant. Retrieving the coherence contribution from the total signal is difficult, but it can be better observed at higher momentum transfer^{44,45} since the transition density is more spread in \mathbf{q} -space (localized in the real-space) while state densities are localized in \mathbf{q} -space (spread across the entire molecule, Fig. S7). Also, the frequency-resolved diffraction can separate the inelastic scattering from the elastic contribution at different Raman-shifts⁴⁵.

The coherence term (v) is separately depicted in Fig. 3c-f along the individual spatial directions, corresponding to a measurement with aligned molecules (3c-e), and the radially averaged axis for a randomly oriented molecule (3f). The phase oscillations between gain (red) and loss (blue) along the temporal and spatial axes are clearly seen in \mathbf{q}_x , \mathbf{q}_y , and \mathbf{q}_z . The temporal oscillations survive the radial averaging (3f) and show the strongest intensities

during the CoIn passage. The spatial information is somewhat concealed here because the q_y and q_z signals exhibit an opposite phase. The observed phase changes correspond to real-space phase changes of the electron density as the molecule crosses the CoIn. This is demonstrated in Fig. 4, where we display the real-space densities: the phase changes at 30, 50, and 61 fs in q -space matches those found in real-space. While we have access to real-space densities in the simulations, they can not be easily extracted from experiment due to the phase problem and the radial averaging. Nevertheless, we have demonstrated that if the coherence term in q -space is extracted, it gives direct information about the real-space phase change of the transition density.

3.3 Discussion

The actual electronic coherence observed in experiments might be weaker or stronger than the predicted one in our simulation due to the absence of the nuclear coordinates describing the S_1 PES. The (in)efficient intersystem crossing might result in (stronger)weaker coherence for TRUECARS signal and geometric phase and the topology of the CoIn may decrease the coherence magnitude.

The realistic pump pulse may not lead to the impulsive excitation as considered in our simulation; part of ground state population would be excited to the S_2 state depending on the molecular nature. For example, uracil has 100% excitation¹⁰ while azobenzene has 80% population transfer⁴⁶. Hence, the observed vibronic coherence magnitude would be weaker than the computed one. For TXRD, there might exist a strong background contribution from unexcited the ground state densities, e.g., ground state bleach.

Similarly, X-ray probe pulse can cause photoionization or Auger decay ensuing population losses due to the presence of the continuum. TRUECARS and TXRD signal primarily depends on parameters: the intensity of the X-ray probe fields, the number of molecules in the X-ray focal volume, etc. The influence of photoionization can reduce the strength of the signal and erode its temporal and spectral resolution. X-ray fluxes should thus be properly optimized so that these competing decay losses will not compromise the resolution provided by the TRUECARS and TXRD technique. The signal strength can be maximized via a suitable choice of the molecule and by optimizing its density in the experiment. Near-resonant probe pulses can be employed to increase the transition probability^{46,47}. Changes in $\langle \alpha(t) \rangle$ due to X-ray photoionization or additional higher-order strong-field interaction and the relevant signal-to-background ratio is discussed in our previous study⁹.

Ultimately, how large the coherences are may be detected by the proposed signals. Especially in TRUECARS, the signal will be observable as long as there is a non-vanishing coherence since it is background-free. If the coherence is too weak, extracting it from the large elastic scattering background in TXRD may be too difficult.

The most popular experimental technique to unravel the conical intersection is currently attosecond time-resolved X-ray absorption spectroscopy (TrXAS). This technique provides an accu-

rate timing of the conical intersection by temporally resolving the absorption spectra as good as 7 femtoseconds [cite Zinchenko 2021, science]. TrXAS can be relatively easily implemented: the broad enough bandwidth single probe pulse covers the core-excited states providing attosecond temporal resolution. But its broad bandwidth does not provide high spectral resolution thus, it is difficult to interpret spectral information for a complex system due to overlapping absorption lines. The proposed TRUECARS technique provides both temporal and spectral resolution of the conical intersection. In addition to timings, the vibronic coherence structure and the transient energy splitting between the adiabatic states can be read from the spectrum. The difficulties in TREUCARS lie in the experimental implementation due to the use of hybrid pulse with a narrowband and a broadband (the phase-matching between them). TXRD technique requires very hard X-ray beams and thus rendering the experiment very difficult. Covariance X-ray diffraction signal by averaging the product of each stochastic signal can be alternatively used for powdered sample⁴⁵. This technique can offer both temporary and spectrally resolved spatial information about the evolution of the transition charge densities during the CoIn passage at a given q . Once all complications are solved, TXRD experiment can actually be performed, spatial images of the electron density around the CoIn are accessible. This spatial information is unique to scattering-based experiments and not accessible with transient absorption or stimulated Raman. We summarize the signal, pulse requirement, spectroscopic information, and difficulties in the experimental implementation in Table 1.

4 Conclusions

We have simulated the TRUECARS and TXRD signals for $S_2 \rightarrow S_1$ CoIn dynamics of 4TU. Quantum nuclear wavepacket dynamics performed on the effective two-dimensional PES provides an accurate picture of the relaxation dynamics and helps unveil this feature in the CoIn passage. The smaller energetic gradient between the S_2 min and the CoIn enables faster nonradiative relaxation in 4TU (67 fs) compared to uracil (186 fs). The frequency-dispersed off-resonant TRUECARS technique selectively probes vibronic coherences that emerge as unique signatures during the CoIn passage. The signal remains visible until the S_2 state is fully depopulated, since the nuclear WP on both S_2 and S_1 PES oscillate between FC, S_2 min, and CoIn. The TRUECARS spectrograms reveal the energy splitting of adiabatic states giving detailed insight into the vibronic coherence structure. This can be employed to manipulate these coherences and thereby control CoIn passages. The off-resonant TXRD signal images the evolving charge densities during the CoIn passage in momentum space, providing a direct connection to real-space images of charge densities at CoIns. The diffraction pattern of the mixed elastic/inelastic scattering from vibronic coherence emerges at the CoIns and shows distinct gain/loss temporal phase-oscillations. This contribution is covered by the stronger elastic scattering from population states, but could be singled out by either looking at high scattering momentum transfer⁴⁴, or by frequency-dispersed detection⁴⁵. Once, the complications are solved, the proposed TRUECARS and TXRD can provide a complementary information (energetic profiles, charge

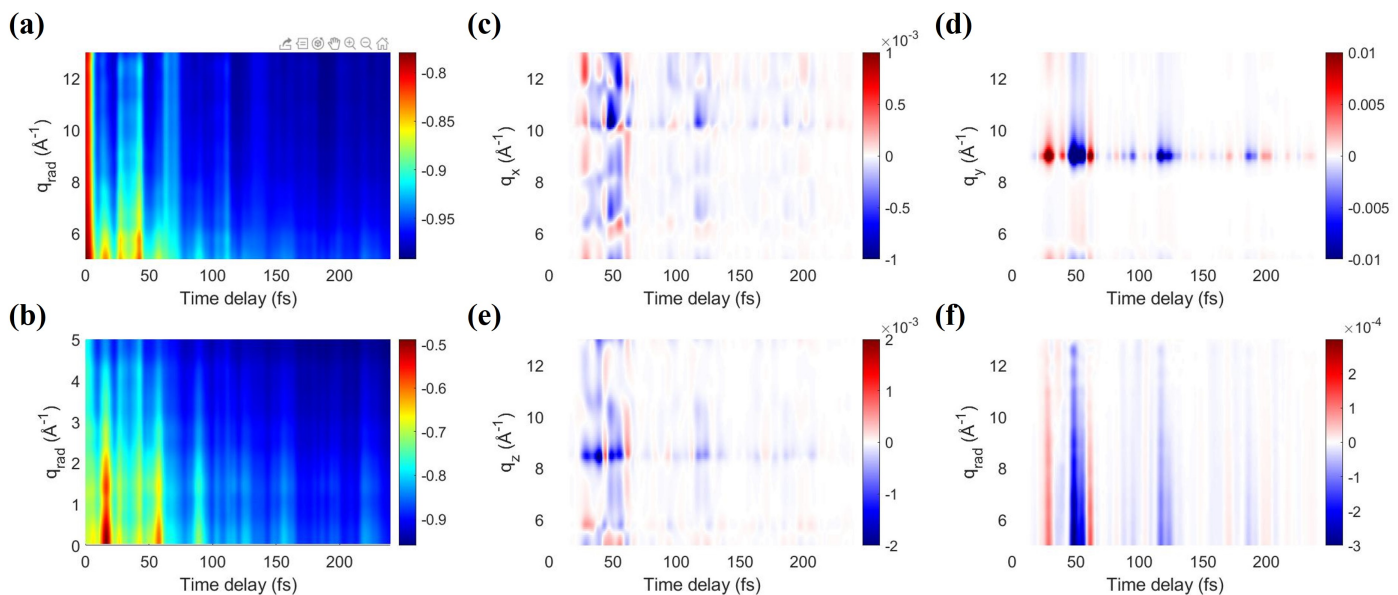


Fig. 3 Normalized time-resolved diffraction signal spread along the different radial momenta (q_{rad}) windows (a, b) and its mixed elastic/inelastic scattering contribution from the vibronic coherence (term (v) in Eq. 9) along (c) q_x , (d) q_y , (e) q_z , and (f) q_{rad} axis. The signals in c–f was represented positive/negative against -1 to emphasize its phase oscillation.

Technique	Signal	Pulse Requirement	Information	Difficulties
TrXAS (established)	$S(\omega_s, T) = -\text{Im} \mu_{\nu} \mu_{\nu}^* \mu_{\nu}^* \frac{e_{\nu}^*(\omega_s) e(\omega_s) \rho_{\nu}(T)}{\omega_s - \omega_{\nu} + i\gamma_{\nu}}$	Single probe pulse (Broad enough)	Precise timing	Difficult to interpret for a complex system
TRUECARS (proposed)	$S(\omega_s, T) = \text{Im} \int dt e^{i\omega_s t} \langle \rho_N(t - T) e^{i\omega_s(t - T)} (\hat{\alpha}^\dagger(t)) \rangle$	Hybrid pulse (Broad/Narrowband)	Energetic profiles vibronic coherence structure Spatial information:	Require two X-ray probe pulses (phase matching)
TXRD (proposed)	$S(\mathbf{q}, T) = N \int dt \mathcal{E}_X(t - T) ^2 \mathcal{S}_1(\mathbf{q}, t)$	Hard X-ray pulse	Electron transition densities around CoIns	Extraction of coherences from the dominant population background

evolution) to decipher the CoIn relaxation pathways which is not possible in the currently used TrXAS technique. The detailed picture of the CoIn passages obtained by TRUECARS and TXRD would be useful to study the underlying photophysics in thiobases.

Author Contributions

Y. N. performed simulations, signal calculations, and analysis, and wrote the original draft. D. K. guided the simulations, signal calculation, analysis and edited the draft. A. N., I. C., F. A., F. S performed the quantum chemistry computations. J. Y. L. administrated the project. M. G. designed the project. S. M. designed, administrated the project and edited the draft.

Conflicts of interest

There are no conflicts to declare.

Acknowledgements

This work was primarily supported by the U.S. Department of Energy, Office of Science, Office of Basic Energy Sciences under Award DE-FG02-04ER15571 (S. M.) and Award DE-SC0019484 (M. G.). The support of the National Science Foundation through Grant No.CHE-1953045 is gratefully acknowledged. Y. N. acknowledges support from the Korea Initiative for fostering University of Research and Innovation Program of the National Research Foundation (NRF) funded by the Korean government (MSIT) (No. 2020M3H1A1077095). D. K. gratefully acknowledges sup-

port from the Alexander von Humboldt Foundation through the Feodor Lynen program

Notes and references

- 1 H. Timmers, Z. Li, N. Shivaram, R. Santra, O. Vendrell and A. Sandhu, *Phys. Rev. Lett.*, 2014, **113**, 113003.
- 2 T. A. A. Oliver, N. H. C. Lewis and G. R. Fleming, *Proceedings of the National Academy of Sciences*, 2014, **111**, 10061–10066.
- 3 A. Raab, G. A. Worth, H.-D. Meyer and L. S. Cederbaum, *The Journal of Chemical Physics*, 1999, **110**, 936–946.
- 4 M. Kowalewski and S. Mukamel, *The Journal of Chemical Physics*, 2015, **143**, 044117.
- 5 A. von Conta, A. Tehlar, A. Schletter, Y. Arasaki, K. Takatsuka and H. J. Wörner, *Nature Communications*, 2018, **9**, 3162.
- 6 L. Young, K. Ueda, M. Gühr, P. H. Bucksbaum, M. Simon, S. Mukamel, N. Rohringer, K. C. Prince, C. Masciovecchio, M. Meyer, A. Rudenko, D. Rolles, C. Bostedt, M. Fuchs, D. A. Reis, R. Santra, H. Kapteyn, M. Murnane, H. Ibrahim, F. Légaré, M. Vrakking, M. Isinger, D. Kroon, M. Gisselbrecht, A. L’Huillier, H. J. Wörner and S. R. Leone, *Journal of Physics B: Atomic, Molecular and Optical Physics*, 2018, **51**, 032003.
- 7 E. A. Seddon, J. A. Clarke, D. J. Dunning, C. Masciovecchio, C. J. Milne, F. Parmigiani, D. Rugg, J. C. H. Spence, N. R. Thompson, K. Ueda, S. M. Vinko, J. S. Wark and W. Wurth, *Reports on Progress in Physics*, 2017, **80**, 115901.
- 8 M. Kowalewski, K. Bennett, K. E. Dorfman and S. Mukamel,

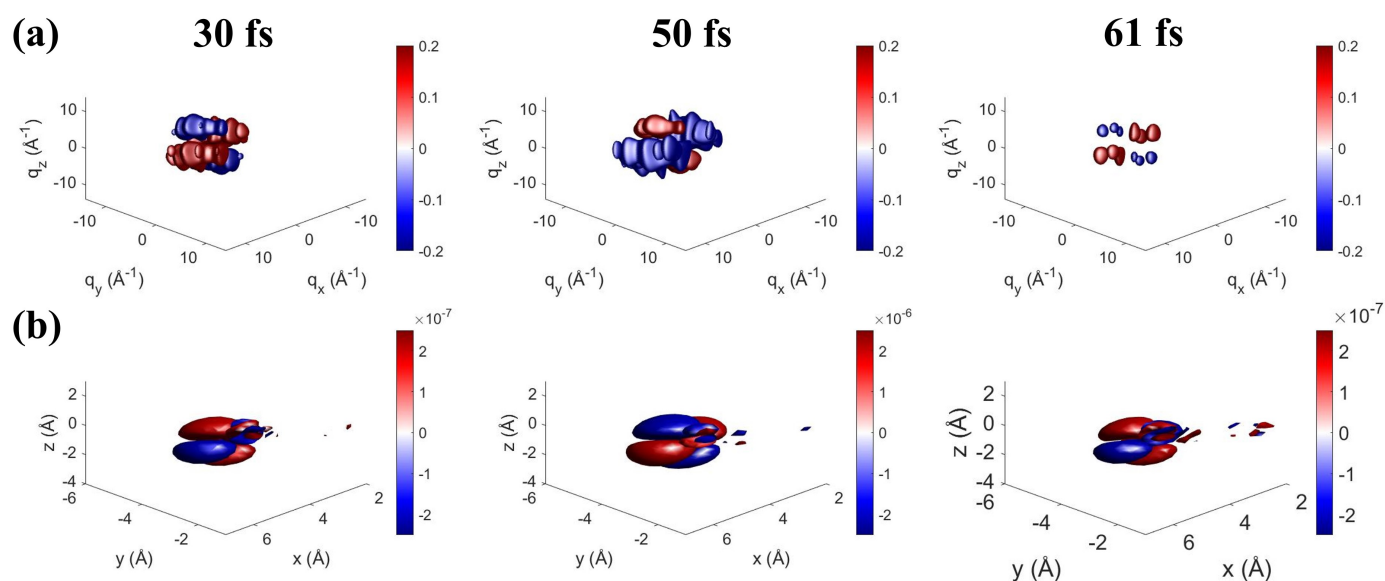


Fig. 4 Three-dimensional snapshots of coherence contribution to the time-resolved diffraction signal in (a) q -space and (b) real-space at 30, 50, and 61 fs.

- Phys. Rev. Lett.*, 2015, **115**, 193003.
- 9 S. M. Cavaletto, D. Keefer and S. Mukamel, *Phys. Rev. X*, 2021, **11**, 011029.
 - 10 D. Keefer, T. Schnappinger, R. de Vivie-Riedle and S. Mukamel, *Proceedings of the National Academy of Sciences*, 2020, **117**, 24069–24075.
 - 11 D. Cho and S. Mukamel, *The Journal of Physical Chemistry Letters*, 2020, **11**, 33–39.
 - 12 D. Cho, J. R. Rouxel and S. Mukamel, *The Journal of Physical Chemistry Letters*, 2020, **11**, 4292–4297.
 - 13 D. Keefer, V. M. Freixas, H. Song, S. Tretiak, S. Fernandez-Alberti and S. Mukamel, *Chem. Sci.*, 2021, **12**, 5286–5294.
 - 14 M. J. J. Vrakking and T. Elsaesser, *Nature Photonics*, 2012, **6**, 645–647.
 - 15 J. M. Glowonia, A. Natan, J. P. Cryan, R. Hartsock, M. Kozina, M. P. Minitti, S. Nelson, J. Robinson, T. Sato, T. van Driel, G. Welch, C. Weninger, D. Zhu and P. H. Bucksbaum, *Phys. Rev. Lett.*, 2016, **117**, 153003.
 - 16 R. J. D. Miller, O. Paré-Labrosse, A. Sarracini and J. E. Besaw, *Nature Communications*, 2020, **11**, 1240.
 - 17 P. Fromme and J. C. Spence, *Current Opinion in Structural Biology*, 2011, **21**, 509–516.
 - 18 J. Küpper, S. Stern, L. Holmegaard, F. Filsinger, A. Rouzée, A. Rudenko, P. Johnsson, A. V. Martin, M. Adolph, A. Aquila, S. c. v. Bajt, A. Barty, C. Bostedt, J. Bozek, C. Caleman, R. Coffee, N. Coppola, T. Delmas, S. Epp, B. Erk, L. Foucar, T. Gorkhover, L. Gumprecht, A. Hartmann, R. Hartmann, G. Hauser, P. Holl, A. Hömke, N. Kimmel, F. Krasniqi, K.-U. Kühnel, J. Maurer, M. Messerschmidt, R. Moshhammer, C. Reich, B. Rudek, R. Santra, I. Schlichting, C. Schmidt, S. Schorb, J. Schulz, H. Soltau, J. C. H. Spence, D. Starodub, L. Strüder, J. Thøgersen, M. J. J. Vrakking, G. Weidenspointner, T. A. White, C. Wunderer, G. Meijer, J. Ullrich, H. Stapelfeldt, D. Rolles and H. N. Chapman, *Phys. Rev. Lett.*, 2014, **112**, 083002.
 - 19 K. Bennett, M. Kowalewski, J. R. Rouxel and S. Mukamel, *Proceedings of the National Academy of Sciences*, 2018, **115**, 6538–6547.
 - 20 S.-K. Son, H. N. Chapman and R. Santra, *Phys. Rev. Lett.*, 2011, **107**, 218102.
 - 21 A. Nenov, I. Conti, R. Borrego-Varillas, G. Cerullo and M. Garavelli, *Chemical Physics*, 2018, **515**, 643–653.
 - 22 R. Borrego-Varillas, D. C. Teles-Ferreira, A. Nenov, I. Conti, L. Ganzer, C. Manzoni, M. Garavelli, A. Maria de Paula and G. Cerullo, *Journal of the American Chemical Society*, 2018, **140**, 16087–16093.
 - 23 M. Pollum, S. Jockusch and C. E. Crespo-Hernández, *Phys. Chem. Chem. Phys.*, 2015, **17**, 27851–27861.
 - 24 D. Keefer, S. Thallmair, S. Matsika and R. de Vivie-Riedle, *Journal of the American Chemical Society*, 2017, **139**, 5061–5066.
 - 25 S. Reiter, D. Keefer and R. de Vivie-Riedle, *Journal of the American Chemical Society*, 2018, **140**, 8714–8720.
 - 26 M. Pollum, L. Martínez-Fernández and C. E. Crespo-Hernández, in *Photochemistry of Nucleic Acid Bases and Their Thio- and Aza-Analogues in Solution*, ed. M. Barbatti, A. C. Borin and S. Ullrich, Springer International Publishing, Cham, 2015, pp. 245–327.
 - 27 M. Pollum, M. Lam, S. Jockusch and C. E. Crespo-Hernández, *ChemMedChem*, 2018, **13**, 1044–1050.
 - 28 C. Reichardt, C. Guo and C. E. Crespo-Hernández, *The Journal of Physical Chemistry B*, 2011, **115**, 3263–3270.
 - 29 A. Favre, G. Moreno, M. Blondel, J. Kliber, F. Vinzens and C. Salet, *Biochemical and Biophysical Research Communications*, 1986, **141**, 847–854.

- 30 K. M. Meisenheimer and T. H. Koch, *Critical Reviews in Biochemistry and Molecular Biology*, 1997, **32**, 101–140.
- 31 I. Fdez. Galván, M. Vacher, A. Alavi, C. Angeli, F. Aquilante, J. Autschbach, J. J. Bao, S. I. Bokarev, N. A. Bogdanov, R. K. Carlson, L. F. Chibotaru, J. Creutzberg, N. Dattani, M. G. Delcey, S. S. Dong, A. Dreuw, L. Freitag, L. M. Frutos, L. Gagliardi, F. Gendron, A. Giussani, L. González, G. Grell, M. Guo, C. E. Hoyer, M. Johansson, S. Keller, S. Knecht, G. Kovačević, E. Källman, G. Li Manni, M. Lundberg, Y. Ma, S. Mai, J. P. Malhado, P. Malmqvist, P. Marquetand, S. A. Mewes, J. Norell, M. Olivucci, M. Oppel, Q. M. Phung, K. Pierloot, F. Plasser, M. Reiher, A. M. Sand, I. Schapiro, P. Sharma, C. J. Stein, L. K. Sørensen, D. G. Truhlar, M. Ugandi, L. Ungur, A. Valentini, S. Vancoillie, V. Veryazov, O. Weser, T. A. Wesolowski, P.-O. Widmark, S. Wouters, A. Zech, J. P. Zobel and R. Lindh, *Journal of Chemical Theory and Computation*, 2019, **15**, 5925–5964.
- 32 J. Finley, P. Åke Malmqvist, B. O. Roos and L. Serrano-Andrés, *Chemical Physics Letters*, 1998, **288**, 299–306.
- 33 P.-O. Widmark, P.-Å. Malmqvist and B. O. Roos, *Theoretica chimica acta*, 1990, **77**, 291–306.
- 34 O. Weingart, A. Nenov, P. Altoè, I. Rivalta, J. Segarra-Martí, I. Dokukina and M. Garavelli, *Journal of Molecular Modeling*, 2018, **24**, 271.
- 35 S. Reiter, D. Keefer and R. de Vivie-Riedle, in *Exact Quantum Dynamics (Wave Packets) in Reduced Dimensionality*, John Wiley Sons, Ltd, 2020, ch. 11, pp. 355–381.
- 36 H. Tal-Ezer and R. Kosloff, *The Journal of Chemical Physics*, 1984, **81**, 3967–3971.
- 37 H.-D. Meyer, F. Gatti and G. A. Worth, in *Basic MCTDH Theory*, John Wiley Sons, Ltd, 2009, ch. 3, pp. 17–30.
- 38 M. Ben-Nun, J. Quenneville and T. J. Martínez, *The Journal of Physical Chemistry A*, 2000, **104**, 5161–5175.
- 39 S. Thallmair, M. K. Roos and R. de Vivie-Riedle, *The Journal of Chemical Physics*, 2016, **144**, 234104.
- 40 S. Butterworth, *Experimental Wireless and the Wireless Engineer*, 1930, **7**, 536–541.
- 41 S. Mukamel and S. Rahav, *Advances in Atomic, Molecular, and Optical Physics*, Academic Press, 2010, vol. 59, pp. 223–263.
- 42 R. Trebino, K. W. DeLong, D. N. Fittinghoff, J. N. Sweetser, M. A. Krumbügel, B. A. Richman and D. J. Kane, *Review of Scientific Instruments*, 1997, **68**, 3277–3295.
- 43 J. R. Rouxel, D. Keefer and S. Mukamel, *Structural Dynamics*, 2021, **8**, 014101.
- 44 D. Keefer, F. Aleotti, J. R. Rouxel, F. Segatta, B. Gu, A. Nenov, M. Garavelli and S. Mukamel, *Proceedings of the National Academy of Sciences*, 2021, **118**, e2022037118.
- 45 S. M. Cavaletto, D. Keefer, J. R. Rouxel, F. Aleotti, F. Segatta, M. Garavelli and S. Mukamel, *Proceedings of the National Academy of Sciences*, 2021, **118**, e2105046118.
- 46 D. Keefer, J. R. Rouxel, F. Aleotti, F. Segatta, M. Garavelli and S. Mukamel, *Journal of the American Chemical Society*, 2021, **143**, 13806–13815.
- 47 J. T. O’Neal, E. G. Champenois, S. Oberli, R. Obaid, A. Al-Haddad, J. Barnard, N. Berrah, R. Coffee, J. Duris, G. Galinis, D. Garratt, J. M. Glowina, D. Haxton, P. Ho, S. Li, X. Li, J. MacArthur, J. P. Marangos, A. Natan, N. Shivaram, D. S. Slaughter, P. Walter, S. Wandel, L. Young, C. Bostedt, P. H. Bucksbaum, A. Picón, A. Marinelli and J. P. Cryan, *Phys. Rev. Lett.*, 2020, **125**, 073203.